Experimental investigation and radial basis function network modeling of direct evaporative cooling systems

Kadir Kavaklioglu [a], Mehmet F. Koseoglu [a,*], Oguz Caliskan [b]

[a] Pamukkale University, Mechanical Engineering Department, Denizli, Turkey
[b] Selcuk University, Mechanical Engineering Department, Konya, Turkey

ABSTRACT

Radial basis function network method is used for modeling a direct evaporative cooling system. Air dry exit temperature, air pressure drop across the cooler and cooler efficiency are predicted using these models. The inputs are pad thickness, air inlet speed, air dry inlet temperature, relative humidity at the inlet and feed water temperature. The data for the models are taken from the experiments performed specifically for this purpose. Model validation is performed using twofold cross validation method. A grid search is used to determine optimal network parameters, such as, optimum number of radial basis elements and spread parameter. Validated models are tested against ordinary least squares models for the output variables. The results indicate that it is feasible to apply radial basis function networks to model direct evaporative coolers.

© 2018 Elsevier Ltd. All rights reserved.

1. Introduction

Evaporative cooling process is an efficient way of cooling and humidification of residential and office buildings as well as some industrial spaces [1,2]. It has found applications in various high-power industrial units, too [3,4]. Water, among widely used working fluids, has the highest latent heat of evaporation, has a very low cost, has no personal and environmental side effects, and is readily available everywhere. Therefore, it has almost become the de facto working fluid for evaporative cooling systems (ECS). Evaporative cooling systems can be divided into three main categories: direct evaporative cooling, indirect evaporative cooling, and indirect-direct evaporative cooling [5]. Direct evaporative coolers in which incoming air stream comes directly into contact with the wetted medium are the subject of this study.

When the water comes into contact with incoming air some evaporation occurs and the energy of evaporation is supplied by the air. As a result, the exit air stream temperature drops and humidity increases because of the added water vapor. The amount of sensible heat removed from the air is equal to the latent heat of evaporation of water which evaporates into air. In the process no net heat is added to or extracted from the whole system; so

entrance and exit states fall on a constant wet bulb temperature line which almost coincides with constant enthalpy line.

According to the standards, there are certain criteria to be used in assessing the performance of direct evaporative coolers [6,7]. Air outlet temperature, pressure drop, and saturation efficiency are three of the most important of them. Air outlet temperature ($T_{out,db}$) is the dry bulb temperature of the moist air at the cooler outlet and is one of the important parameters especially since it is the parameter that the users of ECSs care the most. Pressure drop across the pads (ΔP) is another important performance parameter as it relates to the fan power required to drive the system. Finally, the direct evaporative cooling efficiency (η) is probably the most important performance parameter as it indicates how close a given ECS is to the maximum possible cooling. This efficiency is defined as the actual temperature drop across the ECS divided by the maximum possible temperature drop.

$$\eta = \frac{T_{in,db} - T_{out,db}}{T_{in,db} - T_{in,wb}} \tag{1}$$

Here, $T_{in,db}$ is the dry bulb temperature of the air at the inlet of the ECS, and $T_{in,wb}$ is the wet bulb temperature at the inlet conditions. As mentioned previously, $T_{out,db}$ is the dry bulb temperature of the air mixture at the ECS outlet. Determining these three parameters is essential in evaluating performance of evaporative coolers.

Evaluating these three parameters requires a few additional sensors around the cooler. For instance, air outlet temperature

* Corresponding author at: Pamukkale University, Mechanical Engineering Department, 20070 Kinikli, Denizli, Turkey.
E-mail address: mfkoseoglu@pau.edu.tr (M.F. Koseoglu).

Nomenclature

Symbols

ANN	artificial neural network
c	center vector
C	centers matrix
e	model error
ECS	evaporative cooling system
MLR	multiple linear regression
n	number of hidden elements
N	number of data samples
OLS	ordinary least squares
r	residual
P	pressure
RBF	radial basis function
RBFN	radial basis function network
RMS	root mean squared
RMSE	root mean squared error
T	temperature
x	input variable
x	input vector
X	input matrix
y	output variable
y	output vector

Greek letters

α	MLR coefficients
β	RBFN weights
ϵ	measurement error
ε	effectiveness
ϕ	radial basis function
Φ	radial basis matrix
η	efficiency
σ	spread parameter

Subscripts

db	dry bulb
h	hidden
i	data index
in	inlet
j	input index
k	hidden index
l	learning
out	outlet
t	test
wb	wet bulb

requires a temperature sensor at the outlet, pressure drop requires two pressure sensors at the inlet and the outlet, and cooler efficiency requires wet bulb temperature of the air at the inlet which cannot even be measured directly. As will be seen later in this paper, the models developed in this research will eliminate the need for the sensors at the cooler outlet. This will lead to design simplifications and cost reduction. Since manufacturing costs are crucial for success in the marketplace, it is believed that the findings in this research will be important for the cooler industry. On the other hand, this research will be important for the academic side of the evaporative cooling society. This is mainly because of the difficulties with the wet bulb temperature evaluation. Thermodynamic wet bulb temperature is an important and unique property of a given moist air sample. Many air conditioning applications require the estimate of wet bulb temperature. It is needed in this paper for the calculation of cooler efficiency. Dry bulb temperature and humidity values can be measured easily, however, the same cannot be said for wet bulb temperatures. Calculation of wet bulb temperature requires a trial-and-error procedure since there is no direct analytical expression. By the models developed in this study, the need for iterative wet bulb temperature calculations is completely eliminated. Cooler efficiency is calculated directly in a one-pass function.

Evaporative coolers have been the subject of many analytical, experimental, and modeling studies. In their numerical study, Tavakoli and Hosseini made a 3D laminar flow modeling for cooling pads of evaporative coolers. They obtained relations for saturation efficiency as a function of number of waves and Reynolds number [8]. Khan et al. developed a numerical formulation and validated with simulations for evaporative cooling problems [9]. Similarly, Camargo et al. [10,11] developed a model for simultaneous heat and mass transfer in direct evaporative coolers and they determined the saturation efficiency from the model and compared with on field measurements. They also made a thermoeconomic analysis of evaporative coolers coupled to an adsorption dehumidifier. In another study, Halasz developed a general mathematical model for all evaporative coolers [12]. Dai and Sumathy made a theoretical study on cross flow direct evaporative coolers and determined the effect of some operational parameters like inlet air temperature, humidity, etc. [13]. In a study, Wu et al. obtained a correlation for cooling efficiency from their simplified heat and mass transfer analysis for drip type direct evaporative cooler [14,15]. They also numerically investigated direct evaporative coolers. In their numerical simulation, evaporated water was treated as the mass source for air flow. As a result, they obtained the influences of several parameters (dry and wet bulb temperature, air velocity, and pad thickness) on cooling efficiency. Artificial neural network modeling to predict various performance parameters of a direct evaporative air cooler has been also used [16,17]. In addition to analytical and modeling studies, many experimental work on performance evaluation of evaporative coolers and cooling pads alone have been performed. Malli et al. experimentally determined the performance of widely used cellulosic pads [18]. Similarly, Barzegar et al. conducted an experimental research on cellulosic pads made out of Kraft and Neutral Sulfite Semi Chemical corrugated papers as evaporative media [19]. They concluded that the cellulosic pad made out of Kraft paper with 2.5 mm flute size had the highest performance in comparison with the other cellulosic pads. A regenerative evaporative cooler with finned channels has been produced by Lee and Lee to determine the performance at different operating conditions [20]. Performances of evaporative coolers are investigated for humid climates too. Xu et al. have conducted an experimental study for the possible application of evaporative coolers in greenhouses. They showed that evaporative cooling can be an efficient alternative for greenhouse cooling [21]. In attempts to improve the performance of evaporative coolers for high relative humidity climates and to be able to reach temperatures below wet bulb temperature many experimental and modeling studies have been conducted. Hasan studied four types of indirect evaporative coolers to conclude that cooling air to temperatures lower than the ambient wet bulb temperature is possible [22]. Later, he used a modified version of the ε-NTU method for indirect evaporative cooling and presented an example for a regenerative air cooler case [23]. Jradi and Riffat developed a detailed numerical model of a cross-flow heat and mass exchanger for buildings air-conditioning applications [24]. In addition, they built a rig for experimental validation. They performed parametric studies to achieve optimum cooling system performance.

Through the analysis of the relevant literature, it was observed that the radial basis function networks (RBFN) have not been applied in modeling of the performance parameters of ECSs. RBFNs have been around for more than 20 years [25–27]. They have not lost their popularity, as they have been successfully applied in the areas of photovoltaic module characteristics estimation [28], and annual electricity demand estimation [29]. Mechatronics, predictive controllers, ozone level estimation, concentrating photovoltaics, and image retrieval are some of the other applications in recent years [30–34]. As a type of neural network, a RBFN tries to build a function approximation as a linear combination of some nonlinear basis functions using input-output data [35]. Therefore, there are two major advantages of the models as having the ability to capture nonlinear relationships and being built on data. The advantage of RBFNs over some other neural networks such as multilayer perceptron is that RBFNs do not require an iterative learning phase and are vulnerable to infamous local minima problem. In this paper, RBFN method was used to estimate the performance of an ECS in lieu of the aforementioned three performance parameters. These performance parameters were modeled as functions of cooling pad thickness, air frontal velocity, air inlet dry bulb temperature, relative humidity, and water temperature as input variables.

This paper is organized as follows: Following this introductory section, a description of the system and the experimental setup is given in the next section. Section 3 is about the theory and implementation details of RBFNs. This section describes the network structure, network parameter estimation, and the procedures for model validation and testing. Section 4 is dedicated to results and their discussions. The results are presented in two subsections for narrow and wide-patterned pads, respectively. Also, a summary of all results is presented in this section. Finally, conclusions of this research study are given in the last section.

2. System description and experimental setup

Schematic representation of the experimental set-up is shown in Fig. 1. The test set-up constructed for the experiments consists of an air handling unit, a test room, and a measurement station. The air handling unit in Fig. 2 is an IMEKSAN IKS-25 which has cooling, heating, and humidifying units. It can supply uniform temperature between 15 °C and 45 °C, and relative humidity between 10% and 60%. The maximum air flow rate at the outlet is 5000 m³/h, pressure is 936 Pa, and fan speed is 2999 rev/min. Moisture supply to the system is done with a Devatec ElectroVap MC2 vapor humidifier which has a capacity of 30 kg/h vapor flow rate.

The test room which contains complete evaporative cooling unit or cooling pad has dimensions of 5000 mm × 3000 mm × 6000 mm and has been constructed with sandwich panels which have 80 mm polyurethane foam between two galvanized sheets with 0.5 mm thickness. The thermal conductivity of the polyurethane foam is 0.024 W/m K. Thus, heat loss can be avoided, and uniform temperature and humidity values representing various outside conditions to test direct evaporative coolers can be obtained.

Air flow measuring station is a square duct of 400 mm × 400 mm dimensions, and it has 20 mm thick thermally insulated walls. In the test room, two Testo 6224 radio probes with negative temperature coefficient outside sensors are used to measure the temperature and humidity at the inlet of the cooler. Temperature measurement range of the probes is between −20 °C and +70 °C with an accuracy of ±0.2 °C. Relative humidity accuracy is ±2%. Identical probes are used to measure temperature and relative humidity at the outlet of the cooler in the measurement station
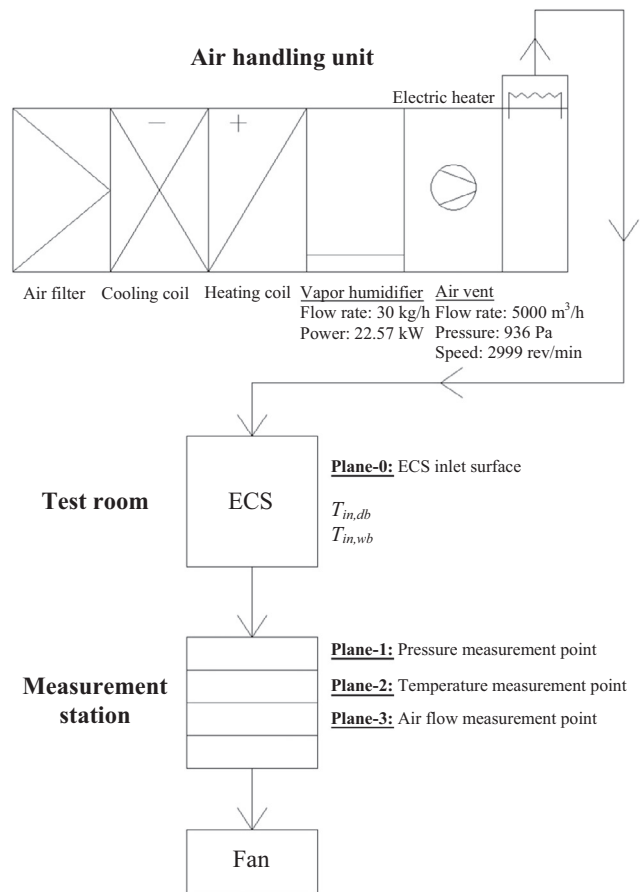

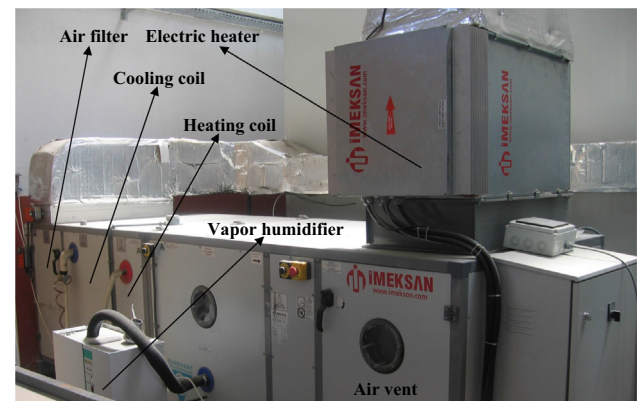**Fig. 1.** Schematics of air handling unit.

Fig. 2. Air handling unit.

in Fig. 3. Water temperature change in the reservoir has been observed with Testo 9222 radio probe with external K-type thermocouple probe with an accuracy of ±0.2 °C. In addition, mercury thermometers are used to measure dry and wet bulb temperatures of the inlet air. In order to measure the pressure drop across evaporative cooling pads, static pressure tabs were flash mounted on duct walls upstream and downstream locations of the pad. Testo 6351 high accuracy differential pressure transmitter with a measuring range of 0–500 Pa, and a measurement accuracy of ±0.3 Pa were used. Frontal air velocity was measured with Testo 4444 air flow transducer with channel type external velocity probe with an accuracy of ±1% of reading. Temperature, humidity, and velocity measurement locations are selected in accordance with the

Fig. 3. Measurement station.

ANSI/ASHRAE 133 Standard [6]. Details of experimental set-up, measurement devices, and techniques have been described in a previous body of work [36]. All the data were collected and processed with a Testo Saveris data acquisition system.

Experiments have been conducted for two of the most widely used cooling pad geometries in industrial evaporative coolers. Narrow cooling pad has a flute height of 5 mm and wide cooling pad has a flute height of 7 mm. Both geometries have a pad angle of 90°. For both geometries experimental data has been obtained for pad thicknesses of 50, 75, 100, 125, 150 mm. An example of cooling pad with primary dimensions are shown below in Fig. 4.

3. Method and theory

3.1. Radial basis function network model

Radial basis function networks are widely used in various disciplines with a good degree of success. This is a result of their excellent ability to do function approximation especially when the relationships among the variables of interest are nonlinear in nature [37,38]. Actually, a radial basis function network is a type of artificial neural network (ANN), and most neural networks are known to be good in modeling complex and nonlinear relationships. An RBFN has advantages in certain applications in that for a given parameter set, RBFN networks do not require an iterative procedure to learn the model. Iterative learning for most ANN
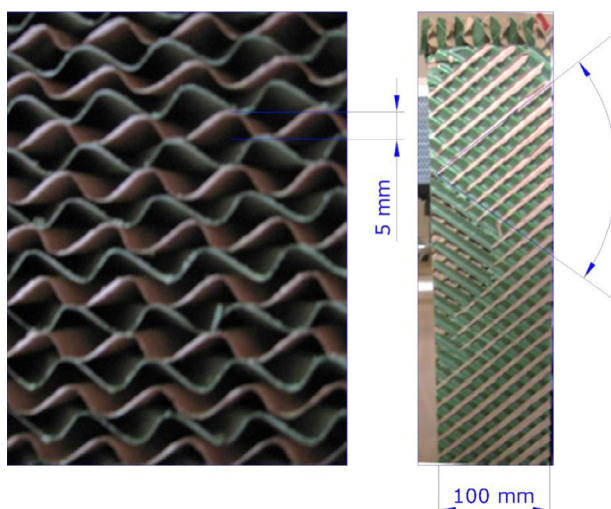
types is computationally expensive and vulnerable to local minima problem.

Topology of a RBFN is given in Fig. 5 as a multiple input single output feedforward network. Assume that there are n input variables labeled from x_1 to x_n. When an input sample is presented to the network, it is represented by a vector $\boldsymbol{x}=[\, x_1 \, x_2 \ldots x_n]$ of size $1 \times n$. The first layer is actually only a buffer that feeds the input values to the middle layer which is called the hidden layer. There are n_h processing elements in the hidden layer. Each processing element in the hidden layer processes the input vector and produces a value as its output. This processing is performed through a basis function ϕ. Among many candidates for basis functions, Gaussian radial basis function (RBF) is used in this study. Main reason for this choice is that, it can be shown that an RBFN with Gaussian RBF can sufficiently approximate any given function for a large enough number of hidden layer elements [38]. This property makes this network a universal aproximator and makes this basis function more commonly used. In this basis, each processing element has a separate vector called the center which has the same dimensions as the input vector. For n_h hidden layer elements we have n_h center vectors as $\boldsymbol{c}_1, \, \boldsymbol{c}_2, \ldots, \boldsymbol{c}_{n_h}$. Then each processing element looks at the distance between the input vector and its center, and uses this distance to create its output. This output takes its maximum value of one when the distance is zero and goes to minimum value of zero as the distance get bigger. The functional form of the Gaussian RBF is given in Eq. (2).

$$\phi(\|\boldsymbol{x} - \boldsymbol{c_k}\|) = \exp\left\{-\frac{\|\boldsymbol{x} - \boldsymbol{c_k}\|^2}{2\sigma^2}\right\}$$

$$= \exp\left\{-\frac{(\boldsymbol{x} - \boldsymbol{c_k})^T(\boldsymbol{x} - \boldsymbol{c_k})}{2\sigma^2}\right\} \qquad (2)$$

Here, σ is called as the spread parameter determining the speed at which the hidden layer outputs goes to zero as the input moves away from centers. Since it is at the denominator, the larger the σ, the slower the outputs go to zero. In literature, one may see slightly different versions of the RBF. In this paper, the form given in Eq. (2) is used due to its conformance with the Gaussian function. After computing all the outputs of the hidden layer, the final output of the RBFN is computed as the linear combination given in Eq. (3):

$$\hat{y}(\boldsymbol{x}) = \beta_0 + \sum_{k=1}^{n_h} \beta_k \phi(\|\boldsymbol{x} - \boldsymbol{c_k}\|) \qquad (3)$$

where the coefficients β_i for $k = 0,1,\ldots,n_h$ are known as the weights of the RBFN.

3.2. Estimation of RBFN parameters

Let us assume that a data set is given as the inputs and outputs to build an appropriate RBFN. Assume that there are N data
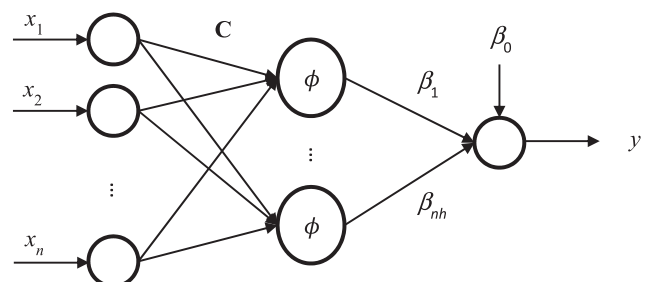

Fig. 4. Dimensions of a cooling pad sample.

Fig. 5. Topology of a RBFN.

samples in the data set. All the input data are represented by the input matrix $\boldsymbol{X}$ and the output data are represented by the output vector $\boldsymbol{y}$:

$$
\boldsymbol{X} = \begin{bmatrix} \boldsymbol{x}^{(1)} \\ \boldsymbol{x}^{(2)} \\ \vdots \\ \boldsymbol{x}^{(N)} \end{bmatrix} = \begin{bmatrix} x_{11} & x_{12} & \cdots & x_{1n} \\ x_{21} & x_{22} & \cdots & x_{2n} \\ \vdots & \vdots & \ddots & \vdots \\ x_{N1} & x_{N2} & \cdots & x_{Nn} \end{bmatrix} \quad \boldsymbol{y} = \begin{bmatrix} y_1 \\ y_2 \\ \vdots \\ y_N \end{bmatrix} \tag{4}
$$

Here $\boldsymbol{x}^{(i)}$ is a $1 \times n$ row vector representing each input sample for $i = 1,2,\ldots,N$. Therefore, each row of input matrix $\boldsymbol{X}$ is an input sample whereas each column represents an input variable. For each of the N rows presented to the network, RBFN is targeted to produce the corresponding element in $\boldsymbol{y}$. Given this data set, designing an RBFN means evaluating the following parameters [38]:

- Number of hidden layer elements: n_h
- Centers for hidden layer elements: $\boldsymbol{C}$

$$
\boldsymbol{C} = \begin{bmatrix} \boldsymbol{c}_1 \\ \boldsymbol{c}_2 \\ \vdots \\ \boldsymbol{c}_{n_h} \end{bmatrix} = \begin{bmatrix} c_{1,1} & c_{1,2} & \cdots & c_{1,n} \\ c_{2,1} & c_{2,2} & \cdots & c_{2,n} \\ \vdots & \vdots & \ddots & \vdots \\ c_{n_h,1} & c_{n_h,2} & \cdots & c_{n_h,n} \end{bmatrix} \tag{5}
$$

- The spread parameter: σ
- Weights: β_k for $k = 0,1,\ldots,n_h$

Determination of the first three parameter sets is usually performed in conjunction with each other as part of model validation procedures and is therefore explained in the next subsection. Only the calculation of weights is explained here assuming that the other parameters are set. For each input sample for $i = 1,2,\ldots,N$, the actual outputs (y_i) may be written as the RBFN outputs ($\hat{y}_i$) plus some measurement error (ϵ_i).

$$
\begin{aligned}
y_1 &= \beta_0 + \beta_1 \phi_1^{(1)} + \beta_2 \phi_2^{(1)} + \ldots + \beta_{n_h} \phi_{n_h}^{(1)} + \epsilon_1 \\
y_2 &= \beta_0 + \beta_1 \phi_1^{(2)} + \beta_2 \phi_2^{(2)} + \ldots + \beta_{n_h} \phi_{n_h}^{(2)} + \epsilon_2 \\
&\vdots \\
y_N &= \beta_0 + \beta_1 \phi_1^{(N)} + \beta_2 \phi_2^{(N)} + \ldots + \beta_{n_h} \phi_{n_h}^{(N)} + \epsilon_3
\end{aligned} \tag{6}
$$

In compact matrix notation, these equations may be written as:

$$
y = \boldsymbol{\Phi}\beta + \epsilon \tag{7}
$$

where

$$
\boldsymbol{y} = \begin{bmatrix} y_1 \\ y_2 \\ \vdots \\ y_N \end{bmatrix}, \quad \boldsymbol{\Phi} = \begin{bmatrix} 1 & \phi_1^{(1)} & \phi_2^{(1)} & \cdots & \phi_{n_h}^{(1)} \\ 1 & \phi_1^{(2)} & \phi_2^{(2)} & \cdots & \phi_{n_h}^{(2)} \\ \vdots & \vdots & \vdots & \ddots & \vdots \\ 1 & \phi_1^{(N)} & \phi_2^{(N)} & \cdots & \phi_{n_h}^{(N)} \end{bmatrix},
$$

$$
\boldsymbol{\beta} = \begin{bmatrix} \beta_0 \\ \beta_1 \\ \beta_2 \\ \vdots \\ \beta_{n_h} \end{bmatrix}, \quad \boldsymbol{\epsilon} = \begin{bmatrix} \epsilon_1 \\ \epsilon_2 \\ \vdots \\ \epsilon_N \end{bmatrix} \tag{8}
$$

A least squares estimation of the weights ($\hat{\beta}$) may be computed using the pseudo inverse as the following:

$$
\hat{\boldsymbol{\beta}} = (\boldsymbol{\Phi}^T \boldsymbol{\Phi})^{-1} \boldsymbol{\Phi}^T \boldsymbol{y} \tag{9}
$$

Finally, the RBFN output may be computed using estimated weights.

$$
\hat{\boldsymbol{y}} = \boldsymbol{\Phi}\hat{\boldsymbol{\beta}} \tag{10}
$$

3.3. Model validation and testing

Number of hidden layer elements (n_h), centers for each hidden layer element ($\boldsymbol{C}$) and the spread parameter (σ) of RBFNs are determined as part of the model validation and testing. Model validation and testing is an essential part of any modeling analysis. It is about finding the model with the best generalization capability given a model topology and a data set. In literature, there are numerous methods proposed to achieve this goal. The basic principle of model validation and testing is to build models using a portion of the available data and assess model quality based on their performance for the data that they have not seen before. In this research, the data set is randomly divided into two groups as learning and test sets. Out of N total data samples, 80% are used for learning (N_l) and the remaining 20% are used for testing (N_t).

The model validation and testing algorithm starts with the simplest possible RBF network by taking the number of hidden layer elements as one. For this case, there is only one center to be found. This center is taken as the centroid of the learning data set. Next step is to determine the spread parameter. For the given pair of n_h and center, 100 different values of σ ranging from 0.1 to 10.0 with the increments of 0.1 are tried. For each σ, first the weight vector $\hat{\beta}$ is found using the least squares method explained in the previous subsection. The vector $\hat{\beta}$ is evaluated using only the learning data which are 80% of the available experimental data that are selected at random. Then for each σ again, RBFN is used to obtain the estimates ($\hat{\boldsymbol{y}}$) for the outputs for the test data set that is the other 20% of the experimental data set. For the test set, actual measured outputs (y_i) and the RBFN outputs ($\hat{y}_i$) are compared to obtain the residual sequence $e_i = y_i - \hat{y}_i$ for $i = 1, 2, \ldots, N_t$. Based on this estimation error, Root Mean Squared Error (RMSE or RMS error) values are calculated for all values of σ when $n_h = 1$ and are recorded for future evaluation.

$$
RMSE = \sqrt{\frac{1}{N_t} \sum_{i=1}^{N_t} e_i^2} \tag{11}
$$

The next step is to increment the number of hidden layer elements by one by setting $n_h = 2$. In this case, there are two centers to be determined where a *k-means clustering* method is used [38]. This method finds two centers in the learning data set and a partition such that the total distance between the data points and their corresponding centers is at minimum. Again, the spread parameter is varied from 0.1 to 10.0 by increments of 0.1 and all the RMSE values are recorded. This loop continues until the number of hidden layer elements reaches its maximum value of N_l which is the number of samples in the training set. At the end of this process, one ends up with a matrix of test RMSE values for all possible pairs of $n_h = 1,2,\ldots,N_l$ and $\sigma = 0.1,0.2,\ldots,10.0$. The best values for the number of hidden layer elements and the spread parameter are decided by taking the pair that has the lowest RMSE. By using this pair of n_h and σ, the final model is fit by determining the centers and the weights using all the available experimental data.

In order to compare validated RBFN model with a basic off-the-shelf model, a multiple linear regression (MLR) model is used.

$$
y = \alpha_0 + \alpha_1 x_1 + \alpha_2 x_2 + \ldots + \alpha_n x_n + \epsilon \tag{12}
$$

This model may be put into the following matrix form:

$$
\boldsymbol{y} = \boldsymbol{X_{MLR}}\boldsymbol{\alpha} + \boldsymbol{\epsilon} \tag{13}
$$

where

$$\boldsymbol{y} = \begin{bmatrix} y_1 \\ y_2 \\ \vdots \\ y_N \end{bmatrix}, \quad \mathbf{X}_{MLR} = \begin{bmatrix} 1 & x_{11} & x_{12} & \cdots & x_{1n} \\ 1 & x_{21} & x_{22} & \cdots & x_{2n} \\ \vdots & \vdots & \vdots & \ddots & \vdots \\ 1 & x_{N1} & x_{N2} & \cdots & x_{Nn} \end{bmatrix},$$

$$\boldsymbol{\alpha} = \begin{bmatrix} \alpha_0 \\ \alpha_1 \\ \alpha_2 \\ \vdots \\ \alpha_n \end{bmatrix}, \quad \boldsymbol{\epsilon} = \begin{bmatrix} \epsilon_1 \\ \epsilon_2 \\ \vdots \\ \epsilon_N \end{bmatrix},$$

$$(14)$$

An ordinary least squares (OLS) estimation of the weights ($\hat{\boldsymbol{\alpha}}$) may be computed using the pseudo inverse as the following:

$$\hat{\boldsymbol{\alpha}} = (\mathbf{X}_{MLR}^T \mathbf{X}_{MLR})^{-1} \mathbf{X}_{MLR}^T \boldsymbol{y} \tag{15}$$

Finally, the MLR output may be computed using estimated weights.

$$\hat{\boldsymbol{y}}_{MLR} = \mathbf{X}_{MLR} \hat{\boldsymbol{\alpha}} \tag{16}$$

4. Results and discussions

As mentioned before, the data used in this research were taken from the experiments performed. RBFN models were built for two types of pads that are labeled as narrow-patterned and wide-patterned pads. There are 5 input and 3 output variables (Table 1) meaning that n is 5.

Since RBFN models are multiple input single output models, a separate model was developed for each of the output variables. There were 120 measurement samples for narrow-patterned pads and 127 measurement samples for wide-patterned pads. All of the computations were performed using an HP Z1 workstation with an Intel Xeon E31245 CPU and 8 GB RAM running Windows 10 Professional 64-bit operating system. MATLAB was used as the computing platform and no toolboxes were used.

4.1. Narrow-patterned pads

4.1.1. Air outlet temperature

Three separate RBFN models for each of the output variables were built using the data for narrow-patterned pads. The first model was for the air outlet temperature (y_1) using 5 input variables ($x_1 \ldots x_5$) listed in Table 1. Out of a total of 119 samples for narrow-patterned pads, 95 randomly selected samples were used for learning and the remaining 24 samples were used for testing. As explained in the theory section, a comprehensive grid search was performed as part of model validation and testing to determine the best model parameters in terms of the number of hidden layer elements and the spread parameter. Naturally, the lower bound for the number of hidden layer elements is one as the

minimum possible number that may happen for RBFN. The upper bound for the number of hidden layer elements is the number of samples in the learning set (N_l). This is because the maximum number of clusters that k-means algorithm can partition out of the learning set is the number of samples in the learning set. Therefore, the range of the number of hidden layer elements in this case is 1–95. As for the range of the spread parameter, 0.1–10 is used with the increments of 0.1. For 95 different values for n_h and 100 different values of the spread parameter, there were 9500 possible pairs of parameters for the RBFN. In the grid search, an RBFN model was built for each pair of parameters by estimating the weights using only the learning data. Then for each pair of parameters and the designed RBFN, the RMSE values were calculated using only the test data that the models have not seen. These 9500 trials took 70.9 s that showed that the design of RBFN models did not take long times since they do not involve iterations and local minima problems. The test RMSE values as a function of the hidden layer size and the spread parameter are presented in Fig. 6.

In terms of the dependence on the number of hidden layer elements, the test RMSE generally decreases at small n_h and increases at medium to high n_h. This is an expected behavior as the ability to fit the data increases by increasing the hidden layer size at small numbers, thereby reducing the test RMSE. After a certain point, this increase in the ability to fit starts to overfit the data and therefore causes the test RMSE to start increasing. Similar discussions can be made on the dependence on the spread parameter. With increasing spread parameter, the test RMSE decreases first and then increases later. For low spread values the radial basis function kernel has a tendency to fit the data points only and decay fast elsewhere. So, increasing the spread in this region will cause better interpolation and generalization performance, and a reduction in the test RMSE. For medium to large spread values, the radial basis function kernel becomes flatter and does not respond to data anymore that lead to the increase in the test RMSE.

Another important observation was made from the results depicted in Fig. 6 based on the region where both the hidden layer size and the spread parameters are large. It was observed that the test RMSE is highly sensitive to both of the parameters in that region. That is to say that small changes in parameters in this region cause wild fluctuations in the model performance. This is called parameter sensitivity and this region should be avoided when selecting parameters. The minimum test RMSE was found to be 0.330 °C and the corresponding optimal RBFN parameters were found to be n_h = 21 and σ = 3.8. The optimum and validated
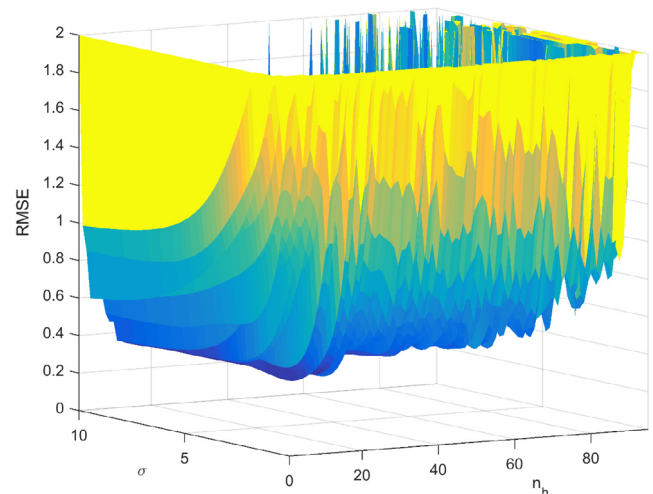
Table 1
List of input and output variables.

Variable	Description	Units	Type
x_1	Pad thickness	cm	Input
x_2	Air velocity	m/s	Input
x_3	Air inlet temperature	°C	Input
x_4	Relative humidity	%	Input
x_5	Water temperature	°C	Input
y_1	Air outlet temperature	°C	Output
y_2	Pressure drop	Pa	Output
y_3	Efficiency	%	Output

Fig. 6. RMSE values for various n_h and spread parameter values for narrow pad study.

RBFN for the air outlet temperature has 21 hidden layer elements and consequently it has 21 center vectors. A portion of the centers matrix is given as the following:

$$\boldsymbol{C} = \begin{bmatrix} \boldsymbol{c}_1 \\ \boldsymbol{c}_2 \\ \vdots \\ \boldsymbol{c}_{21} \end{bmatrix} = \begin{bmatrix} 5 & 1.44 & 37.55 & 19.05 & 21.45 \\ 15 & 1.37 & 38.93 & 18.43 & 21.27 \\ \vdots & \vdots & \vdots & \vdots & \vdots \\ 10 & 2.10 & 36.50 & 19.68 & 20.82 \end{bmatrix}$$

RBFN weights for this case is given as the following:

$$\hat{\boldsymbol{\beta}} = \begin{bmatrix} \hat{\beta}_0 \\ \hat{\beta}_1 \\ \hat{\beta}_2 \\ \vdots \\ \hat{\beta}_{21} \end{bmatrix} = \begin{pmatrix} 23.88 & -5.09 & -1.98 & 2.86 & 2.45 \\ 1.51 & -1.38 & 36.67 & -3.01 & 0.98 \\ -2.69 & 26.25 & -4.07 & -7.99 & -2.27 \\ -44.19 & -0.19 & -4.83 & 21.11 & 4.23 \\ 1.98 & -20.09 \end{pmatrix}^T$$

Using these parameters, the estimation of air outlet temperatures for the whole data set of 119 samples along with the measured values are presented at the bottom portion in Fig. 7. The top portion of this figure presents the residuals (r) that are calculated by taking the difference between the measurements and the estimations. In order to evaluate residual plots, plus and minus three standard deviation bands around the mean are provided as dotted lines.

As evident from this figure, RBFN model performed satisfactorily for the whole data set. The mean of the residuals is extremely close to zero and all the residuals are within six standard deviation band of the mean except for one point. There are five distinct regimes in the data set and the validated RBFN model was able to predict the measured air outlet temperature for every regime. The differences between the RBFN estimations and the measured data are mainly due to model validation procedures. Actually, RBFN methodology allows us to create models that have better match between estimated and measured values. However, since the measurements always have errors, fitting measurements better means fitting measurement noise as well as the relationship among variables. This problem is known as overfitting and should be avoided. However, RMSE should not be too large either as one of the main objectives of modeling is the model accuracy. In order to compare and assess the RBFN RMSE, a MLR model is used as the standard model. MLR model parameters are computed using Eq. (15) and are given as the following:

$$\hat{\boldsymbol{\alpha}} = \begin{bmatrix} -3.64 & -0.56 & 0.62 & 0.51 & 0.07 & 0.54 \end{bmatrix}^T \quad (17)$$
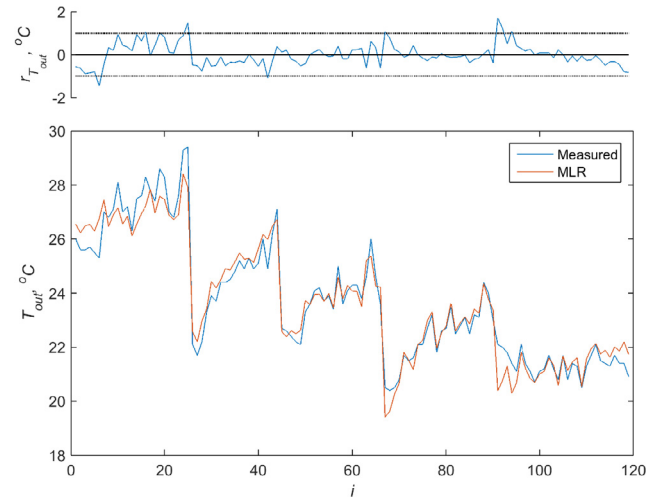
MLR model estimations for air outlet temperature and the measured values are given in Fig. 8 along with the associated residuals.

It is observed from Fig. 8 that MLR model did not perform as well as the RBFN model. Residual mean in this case is close to zero showing that there is not a problem in the mean. However, there are more residuals outside or close to the limits of the six standard deviation band. In fact, the RMSE of the MLR model was found to be 0.512 °C that is 55% larger than that of RBFN model.

4.1.2. Pressure drop

Next in line is the RBFN model for the pressure drop across narrow-patterned pads. All the computational steps for this task is the same as the steps taken for the air outlet temperature. RMSE matrix as a function of hidden layer size and the spread parameter was analyzed and the structure was found to be very similar. The computational time for the model validation phase was found to be 69.9 s which is close to the air outlet temperature value. Minimum test RMSE for the pressure drop model was found to be 3.591 Pa. Optimum hidden layer size was found to be 86 and the spread parameter was found to be 7.4. These values are significantly larger than that of air outlet temperature output variable. This means that there are 86 centers and the radial basis functions are much wider in this case. Estimations from RBFN for the
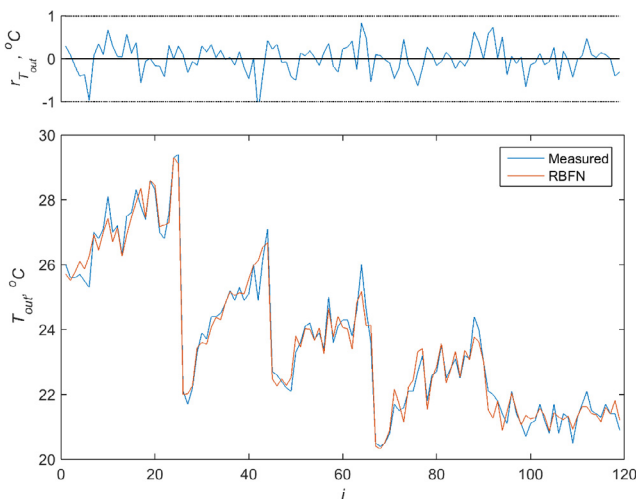

Fig. 8. MLR results using narrow-patterned pad for air outlet temperature.

Fig. 7. RBFN results using narrow-patterned pad for air outlet temperature.
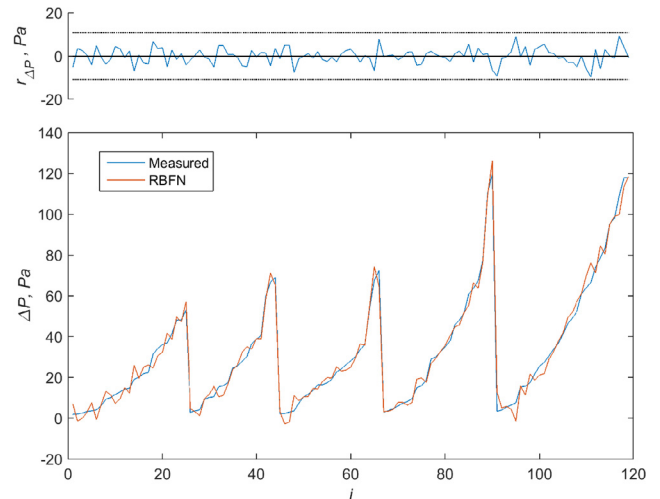

Fig. 9. RBFN results using narrow-patterned pad for pressure drop.

pressure drop are presented in Fig. 9 and the estimations from MLR model are presented in Fig. 10 along with the measured pressure drops. RMSE value for the MLR model was found to be 10.935 Pa which is about three times larger than that of RBFN model. RBFN model residuals are found to be within their bounds, whereas, MLR residuals show significant deviations from their bounds. From these figures, it is observed that RBFN model performed much better than the MLR model across all of the data set. MLR model not only performed poorly, but also produced physically impossible results for some measurement samples. MLR model produced some negative pressure drops for quite a few samples that is less than ideal for any kind of model.

4.1.3. Cooler efficiency

The last output variable for the narrow-patterned pads is the efficiency of the evaporative cooling system. In order to build a validated RBFN model for efficiency same steps as the air outlet temperature and pressure drop were used. RMSE matrix as a function of hidden layer size and the spread parameter was analyzed, and again the structure was found to be very similar to the other variables. The computational time for the model validation phase was found to be 69.5 s which is close to the air outlet temperature and pressure drop values. Minimum test RMSE for the efficiency model was found to be 1.648%. Optimum hidden layer size was found to be 21 and the spread parameter was found to be 3.6. These values are quite similar to that of air outlet temperature output variable and significantly smaller than that of pressure drop variable. This means that there are 21 centers and the radial basis functions are narrower in this case. Estimations from RBFN for the efficiency are presented in Fig. 11 and the estimations from MLR model are presented in Fig. 12 along with the values calculated directly from measurements. RMSE value for the MLR model was found to be 2.983% which is about two times larger than that of RBFN model. Similar to the other estimated variables, RBFN residuals indicate better functional fit compared to the MLR residuals. From these figures, it is observed that RBFN model performed much better than the MLR model across all of the data set.

4.2. Wide-patterned pads

4.2.1. Air outlet temperature

As in the case for narrow-patterned pads, three separate RBFN models were built for wide-patterned pads. The first variable modeled for the wide-patterned pads is the air outlet temperature.
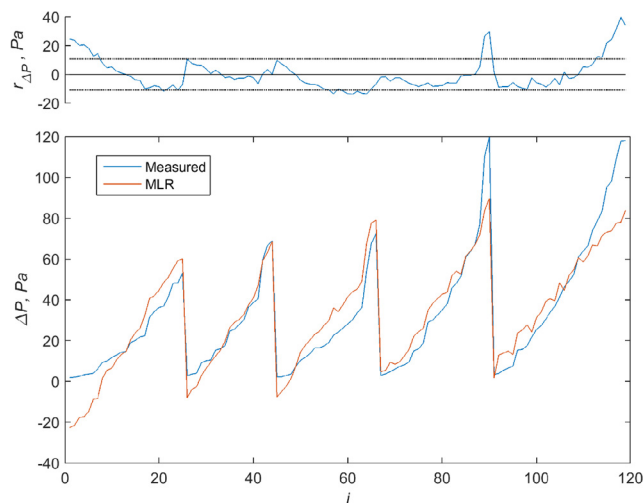

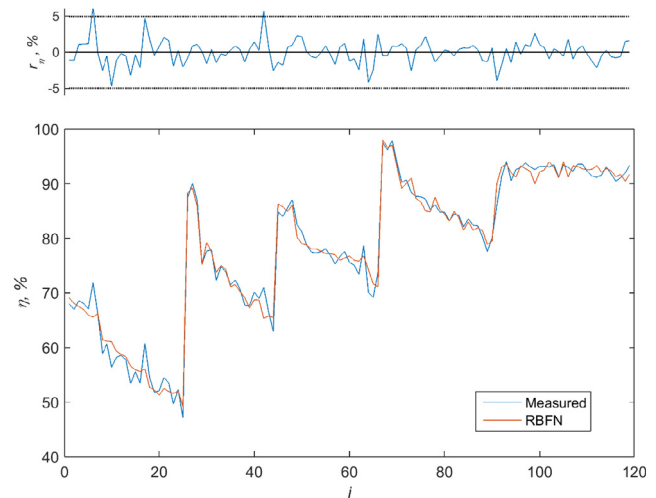**Fig. 10.** MLR results using narrow-patterned pad for pressure drop.

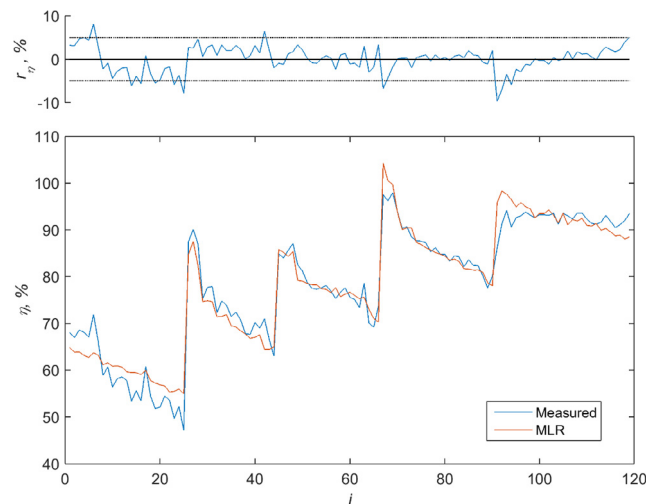**Fig. 11.** RBFN results using narrow-patterned pad for efficiency.

Fig. 12. MLR results using narrow-patterned pad for efficiency.

Total number of data samples for wide-patterned pads was 127. Again, 80% of the total data (102 samples) were used for model learning and the remaining 20% (25 samples) were used for model testing and validation. Therefore, the range of the number of hidden layer elements in this case is 1–102. Same range of the spread parameter is used which is 0.1–10 with the increments of 0.1. For 102 different values for n_h and 100 different values of the spread parameter, there were 10,200 possible pairs of parameters for the RBFN. Computational time for the model validation phase for this variable was found to be 87.9 s which is slightly larger than its narrow-patterned counterpart. This is due to the fact that total number of model trials (10,200) is larger in the wide-patterned case than the narrow-patterned case (9500). RMSE values for this variable as a function of hidden layer element size and spread parameter is given in Fig. 13. This behavior is similar to the RMSE behavior presented for the narrow pad in Fig. 6. The difference is at the parameters where minimum RMSE is achieved. Minimum RMSE is 0.198 °C in this case and the parameters at which this minimum is achieved are $n_h = 38$ and $\sigma = 8.4$. These values are larger than their narrow pad counterparts. MLR model for this case had an RMSE of 0.620 °C which is more than three times larger than that of RBFN as a testament to the function approximation ability of the proposed method.
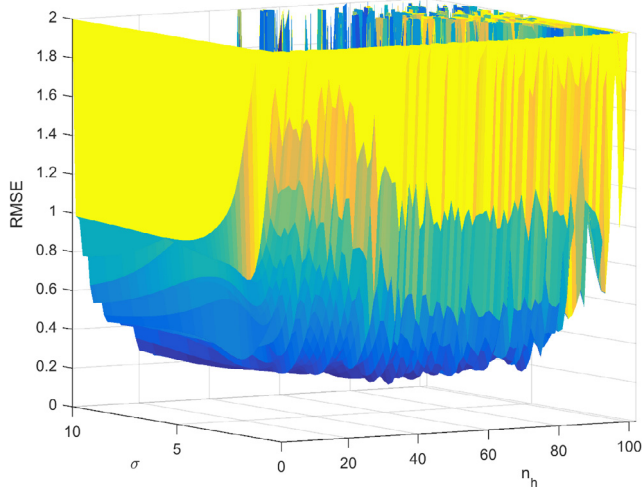
Fig. 13. RMSE values for various n_h and spread parameter values for wide pad study.

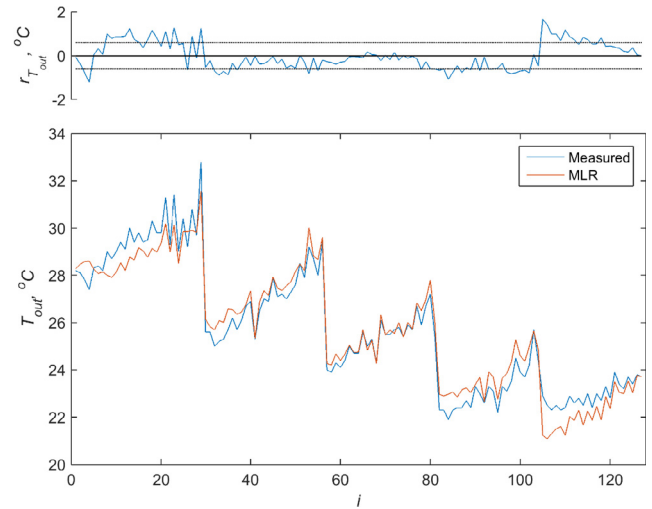**Fig. 15.** MLR results using wide-patterned pad for air outlet temperature.

Validated RBFN model estimations for the air outlet temperature for wide-patterned pads are presented in Fig. 14 along with the measured values. It is evident from the figure that RBFN does a satisfactory job in modeling this relationship. Analysis of residuals for this variable shows that only one residual is outside the six standard deviation band. Results for the MLR model are given in Fig. 15. It is observed that MLR model did not perform as well as the RBFN model.
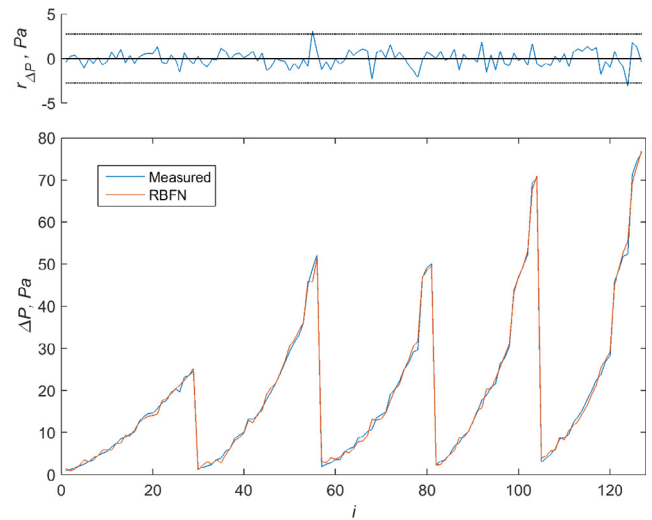
4.2.2. Pressure drop

The second RBFN model for wide-patterned pads is built for the pressure drop across the pad. The computational time for this case was found to be 87.5 s that is close to the time for the other variables. Minimum test RMSE for the pressure drop model was found to be 0.908 Pa. Optimum hidden layer size was found to be 35 and the spread parameter was found to be 2.8. The number of hidden layer elements in this case is close to the value for the air outlet temperature variable. This means that there are 35 centers for the radial basis functions. As indicated in Section 4.1.2, the number of hidden layer elements for pressure drop variable for narrow-patterned pads was 86. It is observed that the number of hidden
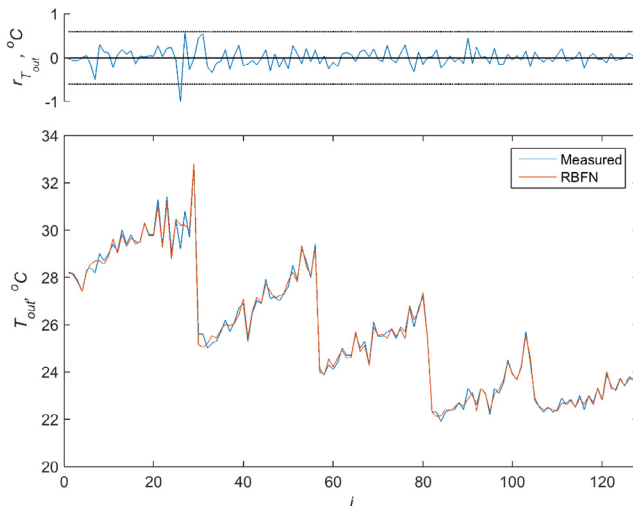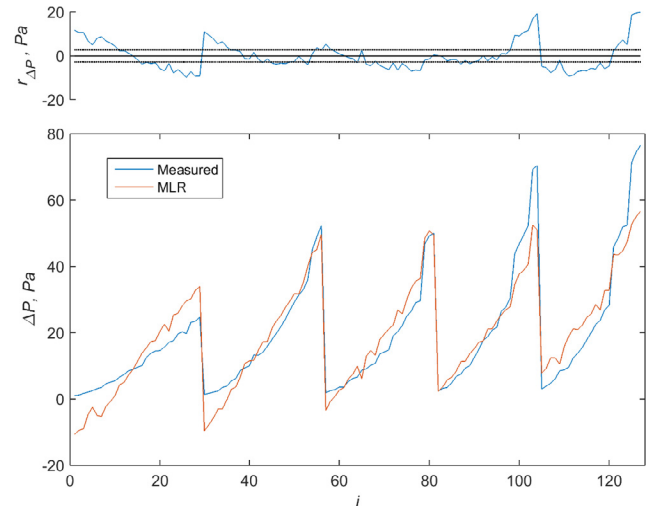

Fig. 16. RBFN results using wide-patterned pad for pressure drop.

Fig. 14. RBFN results using wide-patterned pad for air outlet temperature.

Fig. 17. MLR results using wide-patterned pad for pressure drop.

layer elements for wide-patterned pads are much smaller. Estimations from RBFN for the pressure drop are presented in Fig. 16 and the estimations from MLR model are presented in Fig. 17 along with the measured pressure drops. RMSE value for the MLR model was found to be 6.428 Pa which is about seven times larger than that of RBFN model. RBFN model residuals are found to be within their bounds, whereas, MLR residuals show significant deviations from their bounds. From these figures, it is observed that RBFN model performed much better than the MLR model across all of the data set, again. MLR model not only performed poorly, but also produced physically impossible results for some measurement samples. As it is the case for narrow-patterned pads, MLR model produced some negative pressure drops for quite a few samples that is less than ideal for any kind of model.

4.2.3. Cooler efficiency

The last output variable for the wide-patterned pads is the efficiency of the evaporative cooling system. The computational time for the model validation phase was found to be 87.3 s which is close to the air outlet temperature and pressure drop computational time values. Minimum test RMSE for the efficiency model was found to be 1.095%. Optimum hidden layer size was found to be 38 and the spread parameter was found to be 8.4. These values are same as the values for outlet temperature variable. Estimations from RBFN for the efficiency are presented in Fig. 18 and the estimations from MLR model are presented in Fig. 19 along with the values calculated directly from measurements. RMSE value for the MLR model was found to be 3.450% which is about three and a half times that of RBFN model. Similar to the other estimated variables, RBFN residuals indicate better functional fit compared to the MLR residuals. From these figures, it is observed that RBFN model performed much better than the MLR model across all of the data set.

4.3. Summary of results

For clarity and discussion purposes, all pertinent results are collected in Tables 2–4. First, a summary of all computational time results is given in Table 2. It is observed from this table that computational times are higher for wide-patterned pads and it is caused by the fact that possible maximum number of hidden layer elements in this case is larger. Within a given pad type, computational times do not vary greatly for different output variables.

Next, a summary of all the RMSE results are presented in Table 3. The first observation is that RBFN models outperformed
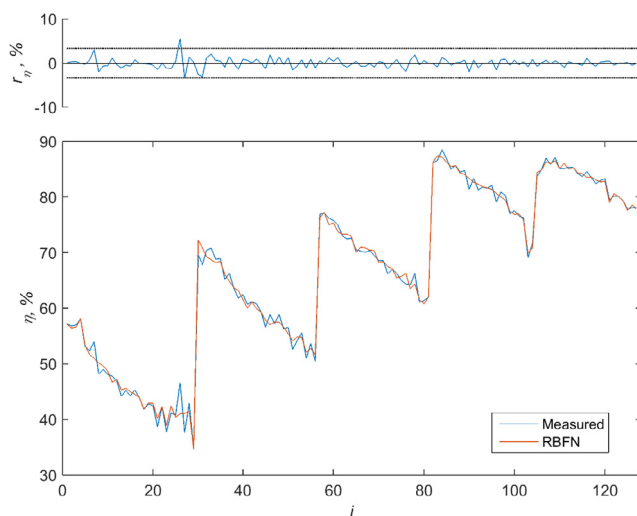

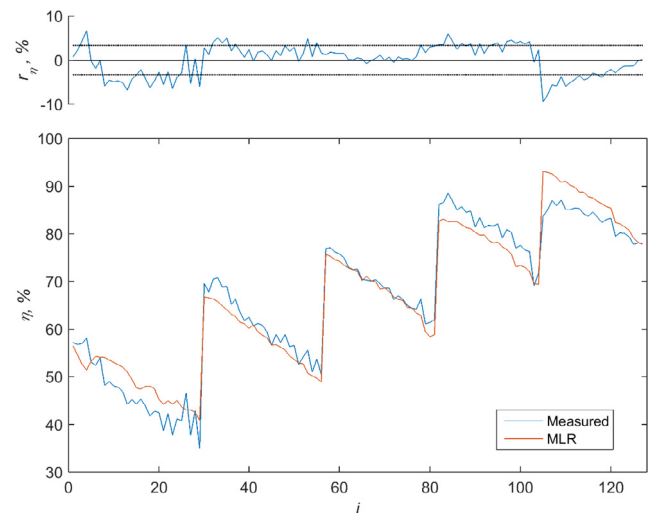**Fig. 18.** RBFN results using wide-patterned pad for efficiency.

Fig. 19. MLR results using wide-patterned pad for air outlet efficiency.

Table 2
Summary of computational time results in seconds.

Output variable	Narrow-patterned pads	Wide-patterned pads
Air outlet temperature	70.9	87.9
Pressure drop	69.9	87.5
Efficiency	69.5	87.3

Table 3
Summary of RMSE results.

Output variable	Narrow-patterned pads		Wide-patterned pads	
	RBFN	MLR	RBFN	MLR
Air outlet temperature (°C)	0.330	0.512	0.198	0.620
Pressure drop (Pa)	3.591	10.935	0.908	6.428
Efficiency (%)	1.648	2.983	1.095	3.450

Table 4
Summary of optimal RBFN parameters.

Output variable	Narrow-patterned pads		Wide-patterned pads	
	n_h	σ	n_h	σ
Air outlet temperature	21	3.8 °C	38	8.4 °C
Pressure drop	86	7.4 Pa	35	2.8 Pa
Efficiency	21	3.6%	38	8.4%

MLR models across the board. In addition, RBFN models are very consistent with the measured data as their RMSE values are small. For instance, 0.33 °C for narrow pads and 0.198 °C for wide pads for air outlet temperature are very well within the measurement accuracy for small scale evaporative coolers. This is evident from Section 2, where the measurement accuracy for temperature sensors are reported as ±0.2 °C. It should also be noted that the RMSE values for RBFN models are consistently smaller for wide-patterned pads than narrow-patterned pads.

Finally, the results for optimal RBFN parameters as the number of hidden layer elements and the spread are summarized in Table 4. It is observed from this table that the numerical values of these two parameters are very close for air outlet temperature and efficiency output variables for narrow-patterned pads. Same can be said for the wide-patterned pads albeit the values are higher.

However, for the pressure drop output variable and for the narrow-patterned pads, the number of hidden layer elements was found to be larger (86). This means that the data complexity for this case presented more challenges for the RBFN, and therefore more and more hidden layer elements needed to be used for validated models.

5. Conclusions

This study investigates radial basis function modeling of performance indicators of direct evaporative cooling systems. The data for this study are taken from the experiments performed on a commercial system. The main conclusion of this research is that it is feasible to use RBFNs for modeling performance indicators of evaporative cooling systems as functions of typically found input measurements. The following are the specific conclusions of this research:

(1) Computational time requirements for RBFN design including model validation and test phases are found to be insignificant. For the models studied in this paper, total times were found to be around 1 min that is a reasonable time period for the given task. Main reason for these small times is the fact that RBFN learning does not require iterations and is not susceptible to local minima. It was found that the computational time is not a function of the output variable or pad type. It is only a function of the size of the learning set.

(2) In terms of the model accuracy, it was concluded that RBFNs are capable of modeling all three performance indicators to a reasonable degree of accuracy. For both types of pads and for all output variables they outperformed the standard MLR models. It was concluded that the RBFN models for wide-patterned pads performed better than the models for narrow-patterned pads. This leads to the conclusion that the functional relationship between input and output variables is more complex for narrow-patterned pads than its wide-patterned counterpart.

(3) Analysis of optimal hidden layer sizes lead to the conclusion that wide-patterned pads require more elements in the hidden layer with the exception of pressure drop variable. It is concluded that the relationship for pressure drop is more complex than other cases.

(4) Analysis of spread parameters lead to the conclusion that the pressure drop variable is again the odd variable for both pad types. Spread parameters for both types of pads differ significantly from the other output variables which also is another indication that pressure drop variable is harder to model than the other two output variables.

The first recommendation for future work for this study is about understanding the model complexity differences between narrow and wide pads. For the pressure drop variable, the numbers of RBFN centers are 86 and 35, for narrow and wide pads, respectively, as reported in the results section. More experiments are needed to understand this difference in model complexity. Another recommendation for future work is a study on the degradation behavior of these pads. The pads used in the experiments are brand new and the models developed are valid for new pads. It would be both academically and industrially important to study how these models change with use in time. The first benefit of this study would be the determination of recalibration intervals for the RBFN models. The second benefit would be to determine the residual life of the pads for replacement schedules. More specifically, it would be desirable to have models for the performance parameters with an additional time-of-service input variable. In addition, it should

be noted that the models developed during this research are specific to the pads used in the experiments. More pad types may be used in the future to enhance the generality of the models developed.

Conflict of interest

The authors declared that there is no conflict of interest

Acknowledgements

Appendix A. Supplementary material

Supplementary data associated with this article can be found, in the online version, at https://doi.org/10.1016/j.ijheatmasstransfer.2018.05.022.

References

[1] G.Q. Qiu, S.B. Riffat, Novel design and modelling of an evaporative cooling system for buildings, Int. J. Energy Res. 30 (2006) 985–999, https://doi.org/10.1002/er.1199.

[2] J. Lee, B. Choi, D.Y. Lee, Comparison of configurations for a compact regenerative evaporative cooler, Int. J. Heat Mass Transf. 65 (2013) 192–198, https://doi.org/10.1016/j.ijheatmasstransfer.2013.05.068.

[3] M. Ameri, H.R. Shahbazian, M. Nabizadeh, Comparison of evaporative inlet air cooling systems to enhance the gas turbine generated power, Int. J. Energy Res. 31 (2007) 1483–1503, https://doi.org/10.1002/er.1315.

[4] A.S. Kaiser, M. Lucas, A. Viedma, B. Zamora, Numerical model of evaporative cooling processes in a new type of cooling tower, Int. J. Heat Mass Transf. 48 (2005) 986–999, https://doi.org/10.1016/j.ijheatmasstransfer.2004.09.047.

[5] S. Anisimov, D. Pandelidis, Theoretical study of the basic cycles for indirect evaporative air cooling, Int. J. Heat Mass Transf. 84 (2015) 974–989, https://doi.org/10.1016/j.ijheatmasstransfer.2015.01.087.

[6] ANSI/ASHRAE 133: ASHRAE Standard, Method of testing direct evaporative air coolers. ASHRAE, Atlanta, 2008.

[7] Australian Standard, Evaporative air conditioning equipment, AS 2913-2000, Standards Australia International, 2000.

[8] E. Tavakoli, R. Hosseini, Numerical analysis of 3D cross flow between corrugated parallel plates in evaporative coolers, Energy Convers. Manage. 52 (2011) 884–892, https://doi.org/10.1016/j.enconman.2010.08.015.

[9] F.A. Khan, C. Fischer, A.G. Straatman, Numerical model for non-equilibrium heat and mass exchange in conjugate fluid/solid/porous domains with application to evaporative cooling and drying, Int. J. Heat Mass Transf. 80 (2015) 513–528, https://doi.org/10.1016/j.ijheatmasstransfer.2014.09.051.

[10] J.R. Camargo, C.D. Ebinuma, J.L. Silveira, Experimental performance of a direct evaporative cooler operating during summer in a Brazilian city, Int. J. Refrig. 28 (2005) 1124–1132, https://doi.org/10.1016/j.ijrefrig.2004.12.011.

[11] J.R. Camargo, C.D. Ebinuma, J.L. Silveira, Thermoeconomic analysis of an evaporative desiccant air conditioning system, Appl. Therm. Eng. 23 (2003) 1537–1549, https://doi.org/10.1016/S1359-4311(03)00105-4.

[12] B. Halasz, A general mathematical model of evaporative cooling devices, Rev. Générale Therm. 37 (1998) 245–255, https://doi.org/10.1016/S0035-3159(98)80092-5.

[13] Y.J. Dai, K. Sumathy, Theoretical study on a cross-flow direct evaporative cooler using honeycomb paper as packing material, Appl. Therm. Eng. 22 (2002) 1417–1430, https://doi.org/10.1016/S1359-4311(02)00069-8.

[14] J.M. Wu, X. Huang, H. Zhang, Theoretical analysis on heat and mass transfer in a direct evaporative cooler, Appl. Therm. Eng. 29 (2009) 980–984, https://doi.org/10.1016/j.applthermaleng.2008.05.016.

[15] J.M. Wu, X. Huang, H. Zhang, Numerical investigation on the heat and mass transfer in a direct evaporative cooler, Appl. Therm. Eng. 29 (2009) 195–201, https://doi.org/10.1016/j.applthermaleng.2008.02.018.

[16] M. Hosoz, H.M. Ertunc, A.F. Ozguc, Modelling of a direct evaporative air cooler using artificial neural network, Int. J. Energy Res. 32 (2008) 83–89, https://doi.org/10.1002/er.1336.

[17] A. Sohani, M. Zabihigivi, M.H. Moradi, H. Sayyaadi, H. Hasani Balyani, A comprehensive performance investigation of cellulose evaporative cooling pad systems using predictive approaches, Appl. Therm. Eng. 110 (2017) 1589–1608, https://doi.org/10.1016/j.applthermaleng.2016.08.216.

[18] A. Malli, H.R. Seyf, M. Layeghi, S. Sharifian, H. Behravesh, Investigating the performance of cellulosic evaporative cooling pads, Energy Convers. Manage. 52 (2011) 2598–2603, https://doi.org/10.1016/j.enconman.2010.12.015.

[19] M. Barzegar, M. Layeghi, G. Ebrahimi, Y. Hamzeh, M. Khorasani, Experimental evaluation of the performances of cellulosic pads made out of Kraft and NSSC corrugated papers as evaporative media, Energy Convers. Manage. 54 (2012) 24–29, https://doi.org/10.1016/j.enconman.2011.09.016.

[20] J. Lee, D.Y. Lee, Experimental study of a counter flow regenerative evaporative cooler with finned channels, Int. J. Heat Mass Transf. 65 (2013) 173–179, https://doi.org/10.1016/j.ijheatmasstransfer.2013.05.069.

[21] J. Xu, Y. Li, R.Z. Wang, W. Liu, P. Zhou, Experimental performance of evaporative cooling pad systems in greenhouses in humid subtropical climates, Appl. Energy 138 (2015) 291–301, https://doi.org/10.1016/j.apenergy.2014.10.061.

[22] A. Hasan, Going below the wet-bulb temperature by indirect evaporative cooling: analysis using a modified ε-NTU method, Appl. Energy 89 (2012) 237–245, https://doi.org/10.1016/j.apenergy.2011.07.005.

[23] A. Hasan, Indirect evaporative cooling of air to a sub-wet bulb temperature, Appl. Therm. Eng. 30 (2010) 2460–2468, https://doi.org/10.1016/j.applthermaleng.2010.06.017.

[24] M. Jradi, S. Riffat, Experimental and numerical investigation of a dew-point cooling system for thermal comfort in buildings, Appl. Energy 132 (2014) 524–535, https://doi.org/10.1016/j.apenergy.2014.07.040.

[25] M.J.D. Powell, Radial basis functions for multivariable interpolation: a review, Chapter 9 in Algorithms for Approximation, Clarendon Press, New York, 1987, pp. 143–167, ISBN: 0-19-853612-7.

[26] S. Chen, C.N. Cowan, P.M. Grant, Orthogonal least squares learning algorithm for radial basis function networks, IEEE Trans. Neural Networks 2 (2) (1991) 302–309, https://doi.org/10.1109/72.80341.

[27] J. Park, I.W. Sandberg, Universal approximation using radial-basis-function networks, Neural Comput. 3 (2) (1991) 246–257, https://doi.org/10.1162/neco.1991.3.2.246.

[28] F. Bonanno, G. Capizzi, G. Graditi, C. Napoli, G.M. Tina, A radial basis function neural network based approach for the electrical characteristics estimation of a photovoltaic module, Appl. Energy 97 (2012) 956–961, https://doi.org/10.1016/j.apenergy.2011.12.085.

[29] S. Yu, K. Wang, Y.M. Wei, A hybrid self-adaptive Particle Swarm Optimization-Genetic Algorithm-Radial Basis Function model for annual electricity demand prediction, Energy Convers. Manage. 91 (2015) 176–185, https://doi.org/10.1016/j.enconman.2014.11.059.

[30] J. de J. Rubio, I. Elias, D.R. Cruz, J. Pacheco, Uniform stable radial basis function neural network for the prediction in two mechatronic processes, Neurocomputing 227 (2017) pp. 122–130. DOI: 10.1016/j.neucom.2016.08.109.

[31] D. Kosic, Fast clustered radial basis function network as an adaptive predictive controller, Neural Networks 63 (2015) 79–86, https://doi.org/10.1016/j.neunet.2014.11.008.

[32] Q.P. Ha, H. Wahid, H. Duc, M. Azzi, Enhanced radial basis function neural networks for ozone level estimation, Neurocomputing 155 (2015) 62–70, https://doi.org/10.1016/j.neucom.2014.12.048.

[33] A.J. Rivera, B. García-Domingo, M.J. Del Jesus, J. Aguilera, Characterization of concentrating photovoltaic modules by cooperative competitive radial basis function networks, Expert Syst. Appl. 40 (2013) 1599–1608, https://doi.org/10.1016/j.eswa.2012.09.016.

[34] G.A. Montazer, D. Giveki, An improved radial basis function neural network for object image retrieval, Neurocomputing 168 (2015) 221–233, https://doi.org/10.1016/j.neucom.2015.05.104.

[35] S.O. Haykin, Neural Networks and Learning Machines, third ed., Pearson, New Jersey, 2008, pp. 239–242. ISBN: 0-13-147139-2.

[36] M.F. Koseoglu, Investigation of water droplet carryover phenomena in industrial evaporative air-conditioning systems, Int. Commun. Heat Mass Trans. 47 (2013) 92–97, https://doi.org/10.1016/j.icheatmasstransfer.2013.07.002.

[37] C.M. Bishop, Pattern Recognition and Machine Learning, first ed., Springer, New York, 2005, pp. 299–303. ISBN: 0-387-31073-8.

[38] S. Theodoridis, K. Koutroumbas, Pattern Recognition, first ed., Academic Press, San Diego, 1999, pp. 120–126, 482-484. ISBN: 0-12-686140-4.